A Generalized Framework for the Performance Evaluation of Microwave Photonic Assisted IR-UWB Waveform Generators

Mohamed Shehata, *Member, IEEE*, Mohamed Sameh Said, *Senior Member, IEEE*, and Hassan Mostafa, *Senior Member, IEEE*

***Abstract*—In this paper, a fast design evaluation approach for microwave photonic (MWP) assisted impulse radio ultrawideband (IR-UWB) waveform generators is presented. The power efficiency (PE) of a photonically generated IR-UWB waveform is the adopted performance evaluation metric of interest, considering two typical waveform types. Analytical expressions are developed for the PE upper bounds of the considered waveforms. The developed expressions have the advantage of being independent of the particular implementation of the photonic generation technique. Accordingly, the PE upper bound of a designed and/or photonically generated IR-UWB waveform can be calculated and optimized *a priori* even if the overall system transfer function is not known. Moreover, the PEs of two practical MWP-based IR-UWB waveform generators are assessed and are compared to the calculated upper bounds. Simulation results validate the applicability of the analytically obtained expressions as upper bounds for the performance of practical MWP-assisted IR-UWB waveform generators.**

***Index Terms*—Impulse radio, microwave photonic (MWP), power efficiency (PE), ultrawideband over fiber (UWBoF).**

I. Introduction

THE ultrawideband (UWB) technology has attracted research interests, especially in high speed short range wireless communications. Although a huge bandwidth is dedicated for UWB signalling, commonly known as the useful UWB band (from 3.1 to 10.6 GHz), the power spectral density (PSD) of an UWB signal is not allowed to exceed the spectral constraints regulated by the Federal Communications Commission (FCC) [1]. The maximum imposed spectral constraint is -41.3 dBm/MHz. This extremely small PSD limit is one of the reasons behind the limited propagation distance of a wirelessly radiated UWB signal. The intensity of a radiated UWB signal is usually expressed in terms of its power efficiency (PE), defined as the ratio of the the power contained in the UWB signal spectrum within the useful UWB band to the total power admissible in this band. Increasing the PE of the emitted IR-UWB waveform extends its wireless reach and secures the minimum signal-to-noise ratio (SNR) requirements at the receiver front end [2]. Recently, the concept of UWB over fiber (UWBoF) network has been proposed to enable the distribution of these signals over optical fibers to remotely located wireless access points. Therefore, microwave photonic (MWP) signal processing techniques have been employed to generate power efficient and FCC compliant UWB signals in the optical domain. In impulse radio UWB (IR-UWB) signalling, the spectrum of a proper basis function, such as a Gaussian pulse, is reshaped by using one or more of three techniques [3]; changing the profile of the basis function, tuning its temporal pulsewidth and differentiating the basis function.

Inspired by the three spectral shaping techniques reported in [3], Wu *et al.* [4] have proposed a theoretical approach for the synthesis of power-efficient IR-UWB waveforms using a multitap finite impulse response (FIR) filter. It has been shown in [4] that the PE of the synthesized waveform increases with increasing the number of the FIR filter taps. A theoretical PE as high as 92.16% has been reported using a multitap FIR filter. Based on this approach, numerous techniques (e.g., [5]–[9]) have experimentally demonstrated the generation of IR-UWB signals using MWP-based multitap FIR filter. These techniques have provided proof-of-concept experiments that partially demonstrate the applicability of the design approach proposed in [4]. However, the compliance of the generated IR-UWB waveforms to the FCC spectral constraints has been the only concern of these techniques, while ignoring the impact of MWP processing on the PE of the resulting waveforms under the FCC spectral constraints. In few other techniques (e.g., [10]), the design parameters of the devices/components involved in the photonic generation process are roughly tuned until a high PE is achieved. As a consequence, optimally produced IR-UWB waveforms are not necessarily guaranteed. On the other hand, many other experimental techniques have been designed within a theoretical framework that accounts for the PE-FCC compliance tradeoff problem. For example, in [11], the theoretical design approach reported in [4] has been followed to experimentally produce IR-UWB waveforms having PEs as high as 75.1% by applying a hyperbolic secant (sech) pulse to a 30-taps all-optical FIR

Manuscript received May 19, 2018; revised October 31, 2018 and January 8, 2019; accepted February 12, 2019. Date of publication March 12, 2019; date of current version November 22, 2019. This work was supported by the National Telecommunications Regulatory Authority of Egypt (NTRA-Egypt). *(Corresponding author: Mohamed Shehata.)*

M. Shehata and M. S. Said are with the Opto-Nano-Electronics Laboratory (ONE Lab), Department of Electrical Engineering, Cairo University, Giza 12613, Egypt (e-mail: m.shehata_ieee@yahoo.com; msmsab@hotmail.com).

H. Mostafa is with the Opto-Nano-Electronics Laboratory (ONE Lab), Department of Electrical Engineering, Cairo University, Giza 12613, Egypt, and also with the Zewail City of Science and Technology, Giza 12588, Egypt (e-mail: hmostafa@uwaterloo.ca).

Digital Object Identifier 10.1109/JSYST.2019.2900699

filter. However, the generation of more power efficient IR-UWB waveforms has been limited by the fabrication complexity of the optical FIR filter [11]. The FIR design in [11] has been improved later in [12] by limiting the number of the FIR filter taps to only eight tap coefficients. Although a theoretical optimum PE of 70.3% has been targeted, the reduced number of FIR filter taps has limited the PE of the resulting IR-UWB waveform to only 63.6%. In [13], a nonlinear genetic algorithm has been employed to optimize the coefficients of the FIR filter in [11] to increase the PE of the resulting waveform, while reducing the number of the FIR filter taps. The optimized coefficients FIR filter has resulted in a maximum PE of 71% using linearly combined sets of non-uniformly delayed pulses that have different pulsewidths. In [14], the number of linearly combined waveforms has been economized to produce an IR-UWB waveform from only two Gaussian doublet pulses. This technique has been further simplified and refined later in [15] to produce an IR-UWB waveform from a linear combination of two monocycles instead of two doublets. Although simple and cost effective, the waveforms reported in [14] and [15] have achieved PEs as low as 12% and 48.52%, respectively. Similarly, in [16], the photonic generation of IR-UWB waveforms having PEs as high as 33.9% and 47.4% have been successfully demonstrated, using a linear combination of three and five monocycle pulses, respectively. The same approach has been improved later in [17] to produce an IR-UWB with a PE of 52.6% from the linear combination of two Gaussian doublet pulses. Recently, the interest in the MWP generation and processing of power efficient IR-UWB waveforms has been directed to the end-to-end performance characterization of complete MWP-assisted UWB transmission systems, with combined optical and wireless transmission [18]–[20].

From the aforementioned overview, it is observed that the attempts to limit the complexity of a theoretical/practical IR-UWB waveform generation technique is accompanied by an inevitable decrease in the PE of the resulting waveform. To the best of the authors' knowledge, no systematic study has been reported to assess the performance limits of MWP-assisted systems, designed for the photonic generation of IR-UWB waveforms. In this paper, a satisfactory balance in the complexity-PE tradeoff of MWP-assisted IR-UWB waveform generators is achieved by economizing the complexity of produced IR-UWB waveforms, while maximizing the *overall* PEs of the resulting waveform. Moreover, closed-form analytical expressions are developed for these performance limits, based on the three spectral shaping techniques introduced in [3], subject to the spectral constraints imposed by the FCC on UWB signals.

The rest of this work is organized as follows. In Section II, the process of photonic generation of IR-UWB waveforms is overviewed and accurately modeled, considering two typical IR-UWB waveform types. Based on this mathematical formulation, Section III presents a proposed analytical approach to calculate the general upper bounds on the PEs of photonically generated IR-UWB waveforms using Schwartz–Holder-Cauchy inequality. The derived analytical expressions are numerically evaluated, analyzed, and optimized in Section IV, considering some time and frequency-relevant design parameters. Then, in Section V, these expressions are applied to two practical designs for MWP-based IR-UWB waveform generators, reported in the literature. In Sections VI and VII, the optimized waveforms obtained in Section IV are compared to some of the power-efficient IR-UWB waveforms reported in the literature, considering their generation-associated computational complexities (CC) and their bit error rate (BER) performances, respectively, as the performance comparison metrics of interest. A number of useful guidelines, to be considered during the design/implementation of practical IR-UWB waveform generators, are provided in Section VIII. Finally, the paper is concluded in Section IX.

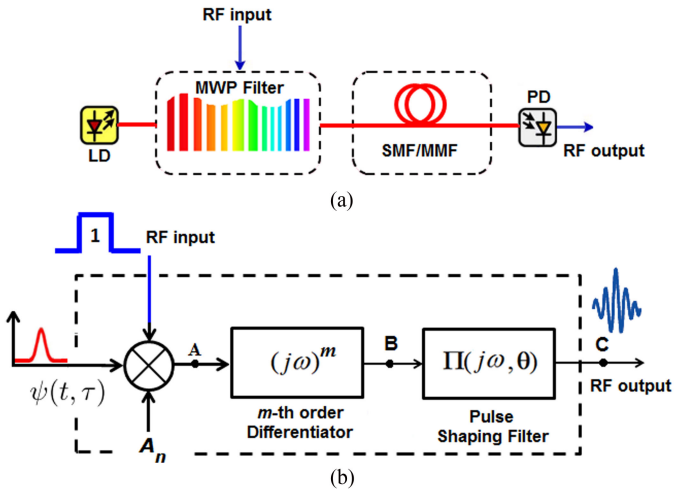

Fig. 1. Typical MWP assisted IR-UWB waveform generator illustrated via (a) a schematic diagram representation and (b) an equivalent block diagram for the system in (a).

Notation: Throughout the rest of the paper, a braced superscript denotes a derivative order, while an unbraced superscript denotes an index.

II. Photonically Generated IR-UWB Waveforms

The photonic generation of IR-UWB waveforms is based on a wide range of optical phenomena exhibited by various MWP components. Fig. 1(a) shows a general schematic diagram representation that illustrates the operation mechanism of MWP-assisted IR-UWB waveform generators. As shown in this figure, a digitally modulated information bearing signal is fed to the radio frequency (RF) input port of the MWP filter, where the RF-optical signal dynamics are excited by the optical signal emitted by a laser diode (LD) to the optical input port of the MWP filter. The optically processed waveform is then propagated down a single mode or a multimode fiber (SMF/MMF) to a remote location, where the received optical signal is transformed to the desired electrical IR-UWB waveform by using a high-speed photodetector (PD).

A. Equivalence Principle

Assuming linearity of the system in Fig. 1(a), the overall transfer function (TF) at the PD output, with respect to the RF

input port, is written as follows:

$$\mathbf{H}(j\omega,\Theta) = H_{\mathrm{MWP}}(j\omega,\Theta_{\mathrm{MWP}}) \times H_{S/\mathrm{MMF}}(j\omega,\Theta_F) \times H_{\mathrm{PD}}(j\omega,\Theta_{\mathrm{PD}}) \quad (1)$$

where $H_{\mathrm{MWP}}(j\omega,\Theta_{\mathrm{MWP}}), H_{S/\mathrm{MMF}}(j\omega,\Theta_F)$, and $H_{\mathrm{PD}}(j\omega,\Theta_{\mathrm{PD}})$ are the complex baseband frequency domain transfer functions of the MWP filter, the SMF/MMF, and the PD, respectively. $\Theta_{\mathrm{MWP}}, \Theta_F$, and Θ_{PD} denote the controllable design parameters of the MWP filter, the SMF/MMF, and the PD, respectively. The parameters involved in the photonic generation process are combined in a single parameters vector, denoted by Θ, where $\Theta = f(\Theta_{\mathrm{MWP}}, \Theta_F, \Theta_{\mathrm{PD}})$. It should be highlighted that the entire photonic generation technique is designed such that $\mathbf{H}(j\omega,\Theta)$ applies three main processing functions to the RF input signal in the optical domain to produce the desired IR-UWB waveform at the PD output. First, the desired differentiation order is applied to an input basis function, denoted by $\psi(t,\tau)$, where τ is a pulse shaping factor that determines the pulsewidth of $\psi(t,\tau)$. Second, the spectrum of the resulting mth order IR-UWB waveform is carefully reshaped such that it does not exceed the FCC spectral mask constraints. Third, the net cumulative optical gain/attenuation along the communications chain, calculated from the RF input port to the PD output, should be adjusted such that that the maximum PSD of the photonically generated IR-UWB waveform does not exceed the maximum FCC PSD limit at the PD output. Fig. 1(b) shows an abstract frequency domain block diagram representation for the functionality of the IR-UWB waveform photonic generation process. Based on the three aforementioned processing functions, $\mathbf{H}(j\omega,\Theta)$ is decomposed into the product of three corresponding frequency domain transfer functions as follows:

$$\mathbf{H}(j\omega,\Theta) = A_n (j\omega)^m \Pi(j\omega,\Theta) \quad (2)$$

where A_n is the net cumulative gain/attenuation from the RF input port to the PD output, $(j\omega)^m$ is the desired mth order frequency domain differential operator and $\Pi(j\omega,\Theta)$ applies additional passive filtering to $A_n(j\omega)^m$, such that the photonically generated waveform at the PD output is fully compliant to the FCC spectral constraints, denoted by $S_{\mathrm{FCC}}(\omega)$. $\Pi(j\omega,\Theta)$ is extracted from $\mathbf{H}(j\omega,\Theta)$ as follows: $\Pi(j\omega,\Theta) = (j\omega)^{-m} A_n^{-1} \mathbf{H}(j\omega,\Theta)$, while A_n is given by

$$A_n = \sqrt{\frac{\max\{S_{\mathrm{FCC}}(\omega)\}}{\max\{|(j\omega)^m \Im\{\psi(t,\tau)\}|\}}}. \quad (3)$$

Accordingly, the resulting frequency domain signal at the PD output [Point C in Fig. 1 (b)] is expressed as follows:

$$\Upsilon(j\omega,\tau) = A_n (j\omega)^m \Im\{\psi(t,\tau)\}\Pi(j\omega,\Theta)\} \quad (4)$$

where $\Upsilon(j\omega,\tau)$ is the Fourier transform of the electrical IR-UWB waveform at the PD output and $\Im\{.\}$ denotes the Fourier transform operation. Consequently, the time-domain IR-UWB waveform at the PD output is calculated by using inverse Fourier transform as follows:

$$y(t) = \Im^{-1}\left\{\Psi^{(m)}_{n,\mathrm{FCC}}(j\omega,\tau)\Pi(j\omega,\Theta)\right\}(t) \quad (5)$$

where $\Im^{-1}\{.\}$ denotes the inverse Fourier transform operation, $\Psi^{(m)}_{n,\mathrm{FCC}}(j\omega,\tau) \triangleq A_n \Psi^{(m)}(j\omega,\tau)$, and $\Psi^{(m)}(j\omega,\tau) = (j\omega)^m \Im\{\psi(t,\tau)\}$.

B. Photonically Generated IR-UWB Pulse Shapes

In many photonic generation techniques, IR-UWB are derived from either a Gaussian [4], [13]–[17] or a sech pulse [11], [21]–[23]. These two common waveform types result from two different and broad categories of photonic generation approaches: The electro-optic (EO) up conversion techniques and the all-optical generation techniques. In EO techniques, an electrical input basis function is impressed on a constant power continuous wave optical carrier. Conventional MWP processing techniques are then applied to the modulated optical carrier to generate the desired IR-UWB waveform. The waveform of the modulating binary input electrical signal is supposed to be a rectangular voltage waveform coupled to the RF input of the MWP generator, usually via a Mach Zhender modulator or an LD. Since UWB systems are designed to provide high signalling data rates, the input basis function resulting from the high speed electrical switching can no longer be represented by a rectangular waveform. Instead, a Gaussian profile better approximates its temporal evolution [2]. On the other hand, in all-optical generation techniques, the modulating RF signal is impressed on ultra-short optical pulses produced by a pulsed optical source, usually a mode locked fiber laser (MLFL), at a rate that is much higher than that of the modulating electrical signal. However, the profile of the pulsed optical electric field produced by an MLFL is best approximated by an ideal sech function [11]. In contrast to the EO techniques, the pulsewidth of the modulating input electrical signal is much greater than that of the ultra-short sech pulse such that the former appears essentially flat. Although rare, some of the reported techniques have adopted other basis functions that possess pulse profiles other than the Gaussian and the sech pulses, such as the super-Gaussian pulse [24], [25]. A generic form of the excitation basis function is expressed as follows:

$$\underset{-\infty\le t\le\infty}{\psi(t,\tau)} = 2\exp\left(-|t/\tau|^p\right)\left(1+\exp(-2q|t/\tau|)\right)^{-1} = \begin{cases} \exp(-t^2/{\tau_g}^2); & \text{for a Gaussian pulse} \\ \mathrm{sech}(t/\tau_s); & \text{for a sech pulse} \end{cases} \quad (6)$$

where $\{p,q\} \in \{0,1,2\ldots\}, \tau = 2\sqrt{\log(2)}\tau_g = 2\mathrm{sech}^{-1}(1/2)$ τ_s, τ_g is the Gaussian pulsewidth, defined as the e^{-1} point of the Gaussian basis function, and τ_s is the pulsewidth of the sech basis function. Table I lists different forms of the generalized basis function $\psi(t,\tau)$ based on different combinations of p. Accordingly, only simple mathematical manipulations are required to adapt the provided analysis to the newly obtained basis functions.

TABLE I
DIFFERENT FORMS OF THE GENERALIZED BASIS FUNCTION $\psi(t,\tau)$ BASED ON DIFFERENT COMBINATIONS OF p AND q

Parameter values (p,q)	Basis function Name	Expression
$(2<p<\infty, q=0)$	Super-Gaussian	$\exp\left(-\lvert t/\tau\rvert^p\right)$
$(p\to\infty, q=0)$	Rectangular	$\mathrm{rect}(t/\tau)$
$(p=2, q=0)$	Gaussian	$\exp\left(-\lvert t/\tau\rvert^2\right)$
$(p=1, q=0)$	Absolute Exponential	$\exp\left(-\lvert t/\tau\rvert\right)$
$(p=1, q=1)$	Sech	$\mathrm{sech}(t/\tau)$

Accordingly, $\Psi^{(m)}_{n,\mathrm{FCC}}(j\omega,\tau)$ is expressed, in terms of the Fourier transform of (6), as follows:

$$\Psi^{(m)}_{n,\mathrm{FCC}}(j\omega,\tau)=A_n\times\begin{cases}(j\omega)^m\tau\sqrt{\pi}\exp\left(\frac{-(\omega\tau)^2}{2}\right)\\ \\ (j\omega)^m 4\pi\tau\mathrm{sech}(2\pi\omega\tau).\end{cases}\tag{7}$$

C. Pulse Amplitude-Pulsewidth Relationship

The spectra of Gaussian and sech-based derivatives are characterized by a unique peak emission frequency ω_p, defined as the frequency at which the spectrum of an mth order derivative pulse attains its global maximum value. In general, for the mth order derivative of Gaussian and sech-based pulses, there is an inverse relationship between the temporal pulsewidth τ and the peak emission frequency of the pulse PSD. The exact form of this relationship depends on the particular pulse shape of the input basis function, its pulsewidth, and particular value of *m*. The $\tau-\omega_p$ relationship is obtained for Gaussian and sech-based IR-UWB waveforms by solving $\partial|\Psi^{(m)}_{n,\mathrm{FCC}}(j\omega,\tau)|^2/\partial\omega=0$ for ω. For Gaussian-based IR-UWB waveforms, the $\tau-\omega_p$ relationship has the form of inverse proportionality as [6]

$$\omega_{p,g}=\frac{\sqrt{2m}}{\tau_g}\tag{8}$$

where $\omega_{p,g}$ is the peak emission frequency of an mth order Gaussian-based IR-UWB waveform. On the other hand, applying $\partial|\Psi^{(m)}_{n,\mathrm{FCC}}(j\omega,\tau)|^2/\partial\omega=0$ to the sech-based IR-UWB waveform defined in (7) yields the following transcendal equation:

$$2\pi\omega_{p,s}\tau_s\tanh(2\pi\omega_{p,s}\tau_s)=m.\tag{9}$$

The peak emission frequency of an mth order sech-based IR-UWB waveform is obtained by using numerical solution techniques to solve (9). The normalization constant in (7) for the Gaussian and sech-based IR-UWB waveforms is expressed, respectively, as follows:

$$A^m_g=\left(S_{\mathrm{FCC}}(\omega)\exp\left((\omega_{p,g}\tau_g)^2/2\right)/(\omega^{2m}_{p,g}\pi\tau^2_g)\right)^{1/2}\tag{10}$$

$$A^m_s=\left(S_{\mathrm{FCC}}(\omega)\cosh^2\left(2\pi\omega_{p,s}\tau_s\right)/(\omega^{2m}_{p,s}(4\pi\tau_s)^2)\right)^{1/2}.\tag{11}$$

In contrast to what is widely done in the literature on the photonic generation of IR-UWB waveforms, where the amplitude of the photonically generated IR-UWB waveform is roughly and independently controlled to achieve compliance with the FCC spectral constraints regardless of the pulsewidth, it is observed from (10) and (11) that the pulsewidth and its amplitude are not independent with the pulsewidth as the key parameter. In other words, the variation in the pulsewidth of the input basis function should be accompanied by a simultaneous variation of the pulse amplitude according to (10) and (11) such that a maximum upper bound of the PE is achieved while respecting the FCC spectral regulations.

III. PE UPPER BOUNDS

The PE of a UWB signal, defined as the percentage contribution of its PSD to the total power dedicated by the FCC for the useful UWB band [15], is the main objective function that should be maximized to obtain optimally energy efficient IR-UWB waveforms. Accordingly, the PE of the IR-UWB waveform in (7) is given by

$$\eta=\frac{1}{\Omega}\int_{\Omega}|\Psi^{(m)}_n(j\omega,\tau)|^2|\Pi(j\omega,\Theta)|^2d\omega\tag{12}$$

where $\Omega\triangleq[\omega_H,\omega_L]$ and $|\Psi^{(m)}_n(j\omega)|^2=|\Psi^{(m)}_{n,\mathrm{FCC}}(j\omega,\tau)|^2/\max\{S_{\mathrm{FCC}}(\omega)\}$. The waveform of the input basis function is often known or at least hypothesized to be analytically modeled with an adequate degree of accuracy. However, there exists numerous forms for $|\Pi(j\omega,\Theta)|^2$, each of which depends on the particular design and implementation of the photonic generation technique. Furthermore, in any of these techniques, it might not be possible to obtain the frequency response of every constituting MWP component in an analytical form. Even if $|\Pi(j\omega,\Theta)|^2$ is given in an analytical form, it might not be always possible to evaluate the integral in (12), due to the mathematical complexity associated with integrals involving the product of Gaussian and sech functions and/or their derivatives with other analytical functions. The problem of finding an upper bound to the PE is substantially simplified by employing Schwartz–Holder-Cauchy inequality [26] to (12) as follows:

$$\eta\le\zeta^m(\tau,\Delta f)\mu(\Theta,\Delta f)\tag{13}$$

where $0\le\Delta f\le(\omega_H-\omega_L)/2\pi$ is defined as the effective bandwidth, or more specifically, the -10 dB bandwidth of the MWP-based waveform generator, and $\zeta^m(\tau,\Delta f)$ and $\mu(\Theta,\Delta f)$ are defined, respectively, as follows:

$$\zeta^m(\tau,\Delta f)\triangleq\left(\frac{1}{\Omega}\int_{2\pi\Delta f\subseteq\Omega}|\Psi^{(m)}_n(j\omega,\tau)|^4d\omega\right)^{1/2}\tag{14}$$

and

$$\mu(\Theta,\Delta f)\triangleq\left(\frac{1}{\Omega}\int_{2\pi\Delta f\subseteq\Omega}|\Pi(j\omega,\Theta)|^4d\omega\right)^{1/2}.\tag{15}$$

To investigate the impact of the MWP waveform generator on the produced waveform, $\Pi(j\omega,\Theta)$ is expressed as an ideal bandpass filter (BPF) whose frequency response is given by $\Pi(j\omega,\Theta)=\mathrm{rect}\left(\frac{\omega-2\pi f_o}{2\pi\Delta f}\right)$, where $\mathrm{rect}(.)$ is the conventional rectangular function, defined as $\mathrm{rect}(x)=1;|x|<1/2,\mathrm{rect}(x)=0;|x|>1/2$, and $f_o=(\omega_L+\omega_H)/4\pi$ is defined as the center frequency of the BPF. Accordingly,

$\mu(\Theta, \Delta f) = 1$ and the PE upper bound is obtained by maximizing only $\zeta^m(\tau, \Delta f)$. Substituting (7) into (14), the PE upper bounds for Gaussian and sech-based IR-UWB waveforms, denoted by $\zeta_g^m(\tau_g, \Delta f)$ and $\zeta_s^m(\tau_s, \Delta f)$, are obtained, respectively, as follows:

$$\zeta_g^m(\tau_g, \Delta f) = \left(\frac{(\pi\tau_g)^2}{\Omega G_p^2} \int_{(\omega_o - \pi\Delta f)\tau_g}^{(\omega_o + \pi\Delta f)\tau_g} \omega^{4m} \exp\left(-(\omega\tau_g)^2\right) d\omega \right)^{1/2} \tag{16}$$

$$\zeta_s^m(\tau_s, \Delta f) = \left(\frac{(4\pi\omega_p\tau_s)^4}{\Omega S_p^2} \int_{(\omega_o - \pi\Delta f)\tau_s}^{(\omega_o + \pi\Delta f)\tau_s} \omega^{4m} \operatorname{sech}^4(2\pi\omega\tau_s) d\omega \right)^{1/2} \tag{17}$$

where $G_p = \omega_{p,g}^m \tau_g \sqrt{\pi} \exp\left(-(\omega_{p,g}\tau_g)^2/2\right)$ and $S_p = 4\pi\omega_{p,s}^m \tau_s \operatorname{sech}(2\pi\omega_{p,s}\tau_s)$. The integrals in (16) and (17) are evaluated analytically and by using numerical integration techniques. The closed-form analytical solution of (16) yields

$$\zeta_g^m(\tau_g, \Delta f) = \left(\frac{\pi^2 \Gamma(2m + 1/2)}{2\Omega G_p^2 \tau_g^{4m-3}} \left[\operatorname{erf}(\mathrm{u}) - \exp(-\mathrm{u}^2) \times \sum_{n=0}^{2m-1} \frac{u^{4m-2n-1}}{\Gamma(2m - n + 1/2)} \right]_{(\omega_o - \pi\Delta f)\tau_g}^{(\omega_o + \pi\Delta f)\tau_g} \right)^{1/2} \tag{18}$$

where $[F(u)]_{u_1}^{u_2} \triangleq F(u_2) - F(u_1)$, $\Gamma(z)$ is the gamma function given by

$$\Gamma(z) = \int_{x=0}^{\infty} y^{z-1} \exp(-y) dy$$

and $\operatorname{erf}(\mathrm{z})$ is the Gaussian error function, given by

$$\operatorname{erf}(\mathrm{z}) = (2/\sqrt{\pi}) \int_0^{\mathrm{z}} \exp(-\mathrm{y}^2) \mathrm{dy}.$$

Similarly, for sech-based IR-UWB waveform, the closed form of the integral in (17) yields

$$\zeta_s^m(\tau_s, \Delta f) = \left(\frac{(16\pi)^3}{2\Omega S_p^2 \tau_s^{4m-3}} \left(\frac{4m!}{(2\pi)^{4m}} \right) [T(u)]_{u_L}^{u_H} \right)^{1/2} \tag{19}$$

where $u_H = 2\pi(\omega_o + \pi\Delta f)\tau_s, u_L = 2\pi(\omega_o - \pi\Delta f)\tau_s$, and T(u) is given by

$$\mathrm{T(u)} = \sum_{q=0}^{4m} \sum_{l=0}^{K} \frac{(-1)^{l-1}(l+1)}{(4m-q)!(2l+4)^{q+1}} u^{4m-q} \exp\left(-2(l+2)u\right).$$

The value of K determines the accuracy of $T(u)$. However, the accuracy of $T(u)$ becomes essentially independent of the particular value of K for $K \gg 10$. Referring to (12), the analytical expressions in (18) and (19) constitute the normalized upper bounds for the PE of Gaussian and sech-based IR-UWB waveforms, respectively.

IV. Simulation Results and Analysis

Throughout simulations, the variation of τ is limited to 300 and 100 ps for Gaussian and sech input basis functions, respectively, whereas the effective system bandwidth Δf is tuned from 0 to 7.5 GHz with a frequency resolution of 1 Hz. $m \in \{1, 2, \ldots, 7\}$. The simulation starts by calculating the angular peak emission frequencies in (8) and (9) as well as their corresponding scaling normalization constants in (10) and (11), respectively. Fig. 2(a) and (b) shows the impact of the simultaneous variation of τ and Δf on $\zeta_g^1(\tau, \Delta f)$ and $\zeta_s^1(\tau, \Delta f)$, respectively. Both figures show that $\zeta_g^1(\tau, \Delta f)$ and $\zeta_s^1(\tau, \Delta f)$ are smooth (i.e., continuous) and concave surfaces. The continuity of both surfaces indicates that there exist various time and/or frequency relevant system design parameters at which either optimal or close-to-optimal upper bounds can be approached by properly controlling these parameters. The optimal sets $(\tau_{g,\mathrm{opt}}^m, \Delta f_{\mathrm{opt}})$ and $(\tau_{s,\mathrm{opt}}^m, \Delta f_{\mathrm{opt}})$ that lead to the optimization of (18) and (19) can be analytically obtained by applying the following two relationships to the closed-form expressions in (18) and (19), respectively,

$$\frac{\partial^2}{\partial\Delta f \partial\tau_g} \zeta_g^m(\tau_g, \Delta f) = 0; 0 \le \tau_g \tag{20}$$

$$\frac{\partial^2}{\partial\Delta f \partial\tau_s} \zeta_s^m(\tau_s, \Delta f) = 0; 0 \le \tau_s. \tag{21}$$

Clearly, the analytical solutions of the multiobjective disjoint optimization problem in (13) are replaced by their equivalents in (20) and (21). However, analytical optimization techniques might be quite difficult to apply. Instead, since the considered ranges of τ and Δf include the optimal PE points of both waveform types, a numerical optimization technique, particularly, the direct search algorithm, is applied over all values of τ and Δf such that the optimized sets $(\tau_{g,\mathrm{opt}}^m, \Delta f_{\mathrm{opt}})$ and $(\tau_{s,\mathrm{opt}}^m, \Delta f_{\mathrm{opt}})$, which are the solutions of (20) and (21), respectively, are obtained. Clearly, there is a global optimum PE of 84.72% achieved by the Gaussian monocycle at $(\tau_{g,\mathrm{opt}}^1 = 50.51$ ps, $\Delta f_{\mathrm{opt}} = 7.5$ GHz) and a global optimum PE of 87.6% achieved by the sech-based monocycle at $((\tau_{s,\mathrm{opt}}^1 = 11.505$ ps, $\Delta f_{\mathrm{opt}} = 7.5$ GHz). Although not illustrated, due to limited space considerations and the need for hyper-geometric plots, the optimized sets $(\tau_{g,\mathrm{opt}}^m, \Delta f_{\mathrm{opt}})$ and $(\tau_{s,\mathrm{opt}}^m, \Delta f_{\mathrm{opt}})$ of $\zeta_g^m(\tau, \Delta f)$ and $\zeta_s^m(\tau, \Delta f)$, respectively, are calculated for $m > 1$. Interestingly, for both waveform types, the PE increases monotonically with the system bandwidth, and tends to its peak value at $\Delta f_{\mathrm{opt}} = 7.5$ GHz $\forall m$. For each waveform type and order m, the calculated optimal PE operating FWHM pulsewidths $\tau_{g,\mathrm{opt}}^m$ and $\tau_{s,\mathrm{opt}}^m$ are used in studying impact of varying Δf on the behavior of $\zeta_g^m(\tau_{g,\mathrm{opt}}^m, \Delta f)$ and $\zeta_s^m(\tau_{s,\mathrm{opt}}^m, \Delta f)$ as shown in Fig. 2(c) and (d), respectively. Both figures show a monotonic increase in $\zeta_g^m(\tau_{g,\mathrm{opt}}^m, \Delta f)$ and $\zeta_s^m(\tau_{s,\mathrm{opt}}^m, \Delta f)$ with Δf. This can be interpreted as follows. The higher is the effective system bandwidth, the more the PSD of the IR-UWB waveform is included within the useful UWB window. Clearly, the similarity

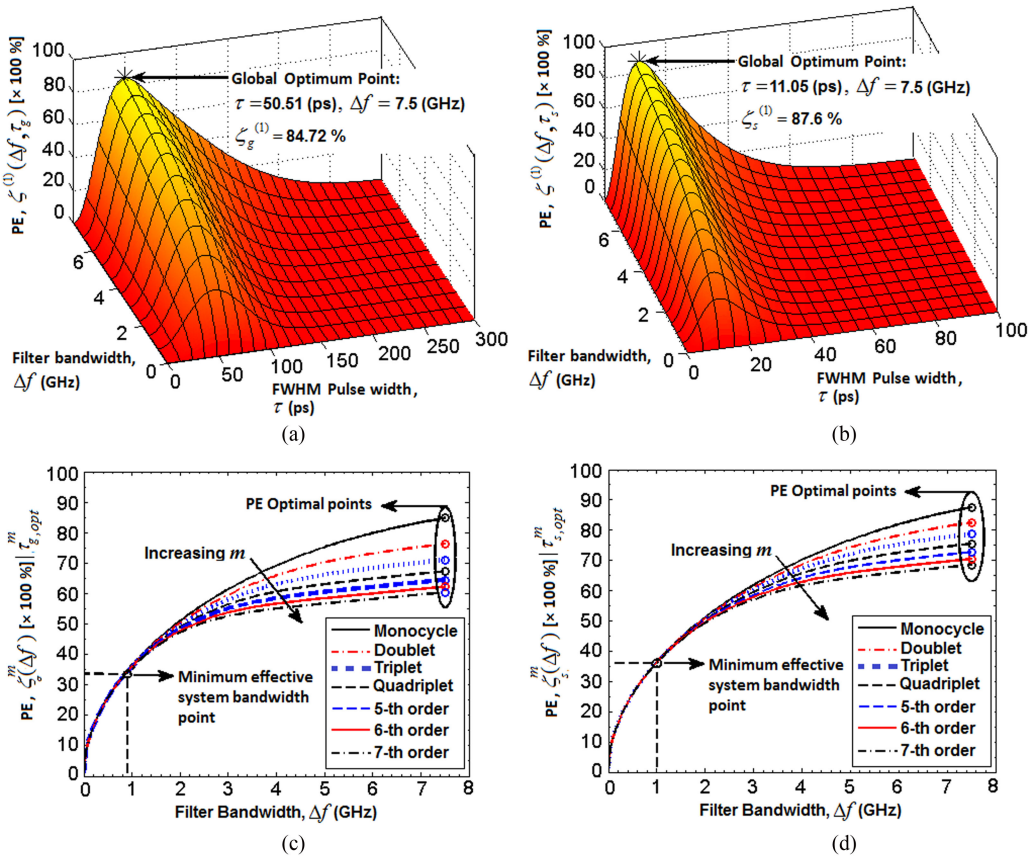

Fig. 2. Normalized upper bounds for the PE versus the effective system bandwidth and the FWHM pulsewidth of the (a) Gaussian monocycle and (b) sech monocycle. Normalized upper bounds for the PE versus the effective system bandwidth at the optimal input FWHM pulsewidth of the first seven derivatives of (c) the Gaussian input basis function and (d) the sech input basis function.

between Gaussian and sech-based IR-UWB waveforms shows an optimality when operating at the maximum effective system bandwidth of $\Delta f = 7.5$ GHz. This is in line with the PE definitions in (12) and (13). On the other hand, there exists a minimum effective system bandwidth below which $\zeta_g^m(\tau_{g,\mathrm{opt}}^m, \Delta f)$ and $\zeta_s^m(\tau_{s,\mathrm{opt}}^m, \Delta f)$ are almost equal for all IR-UWB waveforms of the same type regardless of their order m. For Gaussian-based IR-UWB waveforms, the minimum effective bandwidth is 960 MHz, whereas for sech-based IR-UWB waveforms, this bandwidth should exceed 1 GHz.

Fig. 3(a) and (b) shows the PE upper bounds versus the FWHM pulsewidth of Gaussian and sech-based monocycle pulses, respectively, calculated at $\Delta f = 7.5$ GHz. Obviously, the sech-based monocycle is more sensitive to the variations in the FWHM pulsewidth of the input basis function than its Gaussian-based counterpart. More specifically, the PE of a Gaussian monocycle pulse is achieved at a FWHM pulsewidth that is approximately twice as much the FWHM pulsewidth of a sech monocycle having the same PE. In other words, the IR-UWB waveform generation rate achieved by MWP-assisted filters can be doubled without increasing their bandwidth and/or power penalty requirements if sech-based waveforms are employed. However, PE of a sech-based IR-UWB waveform is also more sensitive to the tolerances and errors in the pulsewidth.

V. Design Examples

In Section III, the entire MWP generator is assumed to produce ideal derivatives of Gaussian and sech basis functions. The analysis of these waveforms, without considering the impact of the residual nonideality transfer function $\Pi(j\omega, \Theta)$, leads to the development of upper bounds for their PEs. In this section, the impact of two particular forms of $\Pi(j\omega, \Theta)$ on the PE of the photonically generated IR-UWB waveform is investigated. Two typical design examples of photonic generation techniques [27] are considered. Fig. 4(a) and (b) shows the implementation approach of each system. The MWP filter in Fig. 4(a) is based on polarization modulation (PolM), while the MWP filter in Fig. 4(b) is implemented using an optical phase modulator (PM). The overall optical frequency domain transfer function of the PolM-based MWP filter is analytically expressed as [27]

$$\mathbf{H}_{\mathrm{PolM}}(\omega) = \left|\cos\left(\frac{\omega\tau}{2}\right)\sin\left(\frac{(\mu + D_G L_{\mathrm{SMF}})\lambda_o^2\omega^2}{4\pi c}\right)\right| \quad (22)$$

whereas the optical frequency domain transfer function of the PM-based system is analytically expressed as [27]

$$\mathbf{H}_{\mathrm{PM}}(\omega) = \left|\sin\left(\frac{\omega\tau}{2}\right)\cos\left(\frac{D_G L_{\mathrm{SMF}}\lambda_o^2\omega^2}{4\pi c}\right)\right| \quad (23)$$

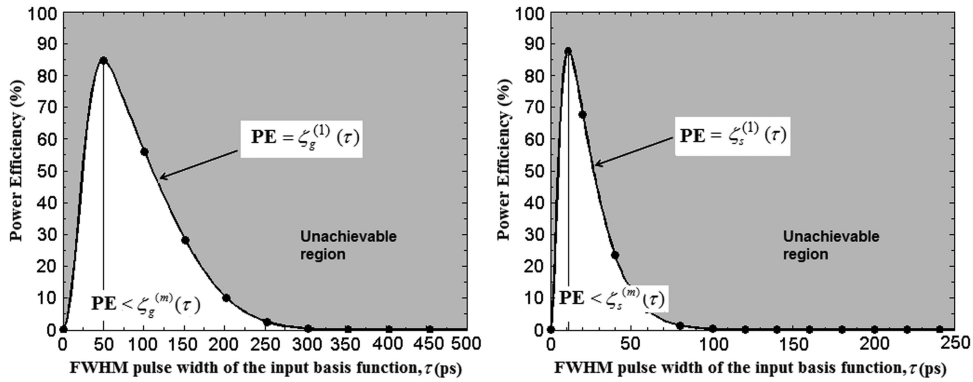

Fig. 3. Normalized PE versus the FWHM pulsewidth of the input basis function for (a) the Gaussian monocycle pulse and (b) the sech monocycle pulse with $\Delta f = 7.5$ GHz. Solid lines: Theoretically obtained values. Markers: Values obtained from numerical simulations. Gray areas represent the unachievable values of the normalized PE.

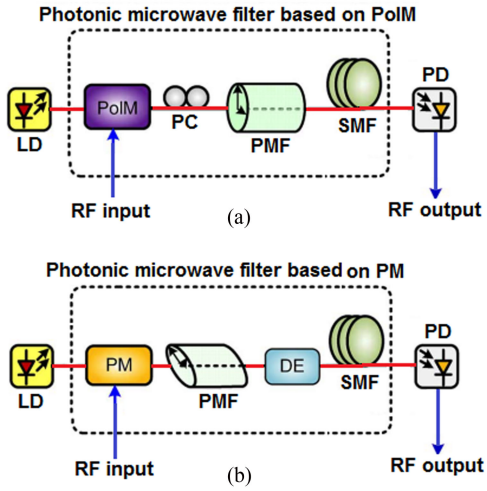

Fig. 4. Design examples of photonic generation of a monocycle pulse using an MWP BPF based on (a) a PolM and (b) a PM.

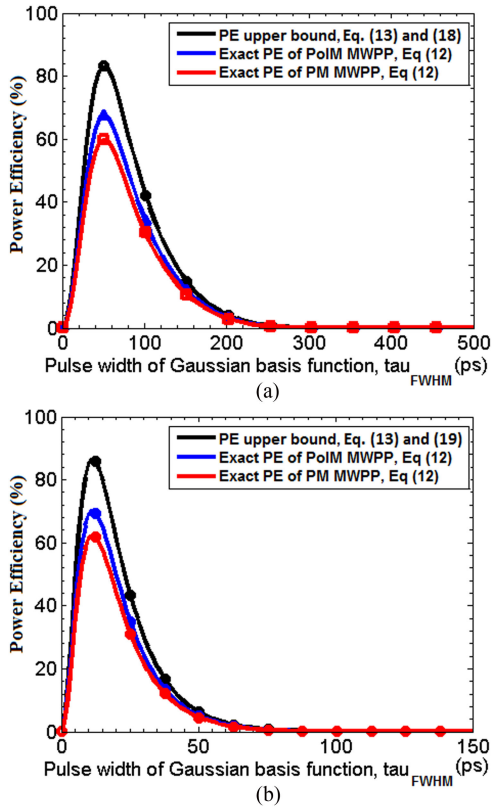

Fig. 5. Comparison of the exact value of the PE as calculated from (12) and its upper bound as calculated from (a) (18) for a Gaussian monocycle pulse and (b) (19) for a Sech monocycle pulse, based on PolM and PM.

where $\tau = 40$ ps denotes the differential group delay of the polarization maintaining fiber, $D_G = 16.5$ ps/nm/km is the group velocity dispersion of the SMF, $L_{\text{SMF}} = 10$ km is the length of the SMF and $\mu = 609$ ps/nm is the dispersion coefficient of the dispersion element in Fig. 4(b). In contrast to [27], where both systems have been designed to generate a Gaussian monocycle pulse with a fixed FWHM pulsewidth, in the present analysis, it is assumed that both Gaussian and sech basis functions, with tunable FWHM pulsewidths, are applied to each of these system inputs, such that Gaussian and sech monocycle pulses are produced, respectively. The applicability of (13) to the considered systems is validated as follows. First, the particular implementation of each system, expressed in terms of (22) or (23), is ignored by substituting $\mu(\Theta, \Delta f) = 1$, along with (18) or (19), into right-hand side of (13) to calculate the upper bound of η. Second, the actual PE values achieved by each system are calculated using (12), which is the same as the left-hand side of (13), and each of the transfer functions in (22) or (23). Fig. 5(a) plots the upper bound of η, along with its actual values, versus the FWHM pulsewidth of a Gaussian input basis function, considering the transfer functions in (22) and (23). Similarly, Fig. 5(b) plots the upper bound of η, along with its actual values, versus the FWHM pulsewidth of a sech input basis function, considering the same transfer functions in Fig. 5(a). As expected, for each waveform type, the PE upper bounds predicted by (13), without the knowledge of the transfer functions of the considered systems, enclose the actual PE values calculated using (12) for both systems. Moreover, in both figures, the global maximum values of the PE values

and their corresponding global maxima located on the upper bounds are achieved at the same optimum FWHM pulsewidths. Furthermore, the difference between an actually achieved PE value and its corresponding upper bound is mainly attributed to the passive filtering effects introduced by $\Pi(j\omega, \Theta)$ through $\mu(\Theta, \Delta f)$, which are not included in PE upper bounds calculated from (13). These results validate the applicability of the PE upper bounds in (18) and (19) to arbitrarily implemented MWP-assisted IR-UWB waveform generators when the targeted waveform type and its FWHM pulsewidth are the only available knowledge.

VI. Complexity Analysis

Based on (2), the CC of $\mathbf{H}(j\omega, \Theta)$ is mainly determined by the individual implementation complexities of the transfer functions $(j\omega)^m$ and $\Pi(j\omega, \Theta)$. In some techniques, the IR-UWB waveform generator is excited by the basis function $\psi(t, \tau)$, and the desired derivative of $\psi(t, \tau)$ is approximated by its corresponding differencing operator [7]. For instance, in [8], the Gaussian monocycle and doublet pulses have been approximated by the first and the second order differences of a Gaussian pulse, respectively. Applying an Nth order differencing operator to an input basis function is implemented by a multitap FIR filter, whose impulse response is modeled as follows:

$$h_{\text{FIR}}(t) = \sum_{k=0}^{N-1} a_k \delta(t - k\Delta T) \tag{24}$$

where a_k are the FIR filter coefficients, $\delta(t)$ is the Dirac-delta function, ΔT is the time delay difference between two adjacent taps, and N is the number of taps. Accordingly, the frequency response of an N-tap MWP FIR filter is given by the Fourier transform of (24) as [7]

$$H_{\text{FIR}}(j\omega) = \sum_{k=0}^{N-1} a_k \exp\left(-jk\omega\Delta T\right). \tag{25}$$

On the other hand, some other techniques (e.g., [4], [14]–[17]) hypothesize the existence of the desired derivative at the input of the IR-UWB waveform generator. In these techniques, $\mathbf{H}(j\omega, \Theta)$, and consequently, its complexity, is determined only by $\Pi(j\omega, \Theta)$. Despite this apparent reduction in the CC, due to excluding $(j\omega)^m$, the transfer function $\Pi(j\omega, \Theta)$ is also implemented by the multitap FIR filter approach. In this case, $H_{\text{FIR}}(j\omega)$ is designed to achieve the required compliance to the FCC spectral constraints by the proper control of the tap coefficients a_k. Accordingly, the order of (25) as well as the derivative order of the exciting waveform determines the CC of both types of IR-UWB waveform generation techniques. Table III compares the CCs, expressed in terms of the number of floating point operations (flops) (additions and/or multiplications), required by the FIR filters to produce IR-UWB waveforms with the PEs reported in [11]–[17].

Fig. 6(a) and (b) shows the PEs achieved by a linear combination of *N* Gaussian-based monocycle pulses in [4] as compared to the PE achieved by the single derivative order Gaussian and sech-based IR-UWB waveforms, respectively. This comparison

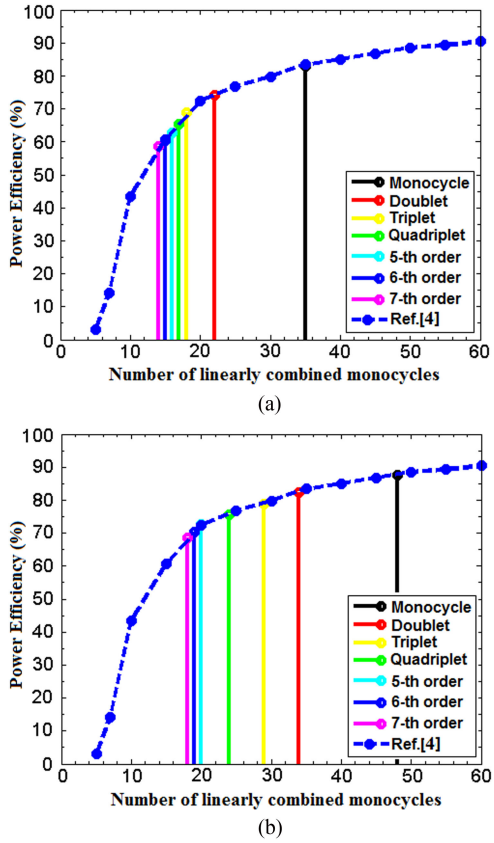

Fig. 6. Comparison of the PE of a linear combination of Gaussian monocycle pulses in [4] with the PE of a single-order pulse having an optimized pulsewidth and derived from (a) a Gaussian basis function and (b) a sech basis function.

TABLE II
Complexity and PE Comparisons of the Proposed Optimal Waveforms to the Waveforms Proposed in [11]–[17]

Ref. No.	Input pulse type	Computational Complexity (flops)	PE [%]
[11]-Design 1	Sech	5	0.12
[11]-Design 2	Sech	7	1.38
[11]-Design 3	Sech	15	47.5
[11]-Design 4	Sech	29	67
[11]-Design 5	Sech	61	75.1
[12]	Gaussian	17	70.3
[13]	Gaussian	17	71
[14]	Gaussian doublet	5	12
[15]	Gaussian monocycle	5	48.52
[16]-Design 1	Gaussian monocycle	7	33.9
[16]-Design 2	Gaussian monocycle	11	47.4
[17]	Gaussian doublet	5	52.6
This work-1	Gaussian	3	84.72
This work-2	Sech	3	87.6

is also provided in Table III for more illustration. Generally, the waveform types and their corresponding PEs listed in Tables II and III emphasize the impact of optimizing the pulsewidth of an IR-UWB waveform on the complexity and PE of this waveform. In Table I, it is clear that an IR-UWB waveform of order m with the proper pulsewidth possesses the same PE achieved by linearly combining a larger number of monocycles using the

TABLE III
COMPLEXITY OF GENERATING THE PROPOSED PULSES WITH THE SAME PEs AS IN [4]

Pulse order, m	Monocycle	Doublet	Triplet	Quadruplet	5^{th} order	6^{th} order	7^{th} order
PE of Gaussian-based [This work]	84.72%	74.1%	68.91%	65.33%	62.58%	60.33%	58.58%
Computational Complexity (flops) [This work]	3	5	7	9	11	13	15
Computational Complexity (flops) based on [4]	71	45	37	35	33	31	29
PE of sech-based [This work]	87.6%	82.44%	78.71%	75.45%	72.73%	70.45%	68.51%
Computational Complexity (flops) [This work]	3	5	7	9	11	13	15
Computational Complexity (flops) based on [4]	97	69	59	49	41	39	37

FIR filter design proposed in [4]. As a particular example, a PE of 84.72% is achieved by a single Gaussian monocycle pulse that has an optimized FWHM pulsewidth, while in [4], the same PE is achieved by using a linear combination of 35 Gaussian monocycle pulses. A higher PE of 87.6% is achieved by a single sech monocycle pulse. This reduces dimensionality of the IR-UWB waveform optimization problem and, consequently, the implementation complexity of the MWP filter in the IR-UWBoF system design if a single-order IR-UWB waveform is targeted. Moreover, it can be correctly concluded that the PE of a linear combination of pulsewidth optimized IR-UWB waveforms converges more rapidly with a lower number of linearly combined pulses as compared to [4].

VII. BER PERFORMANCE ANALYSIS

In practical IR-UWB systems, the information symbols are encoded by the photonically generated IR-UWB waveforms, which are then wirelessly transmitted to a remotely located UWB receiver. Most often, the frequency response of the wireless transmission channel is modeled by the Friis formula for free space path loss (FSPL) channels [13]. In addition to the FSPL, at the receiver front end, the received IR-UWB waveform is unavoidably corrupted by a zero-mean additive white Gaussian noise (AWGN) random process. The higher is the PE of the emitted IR-UWB waveform, the higher is the signal-to-noise ratio (SNR) at the receiver side and consequently, the better is the end-to-end BER performance. In this context, each binary information symbol is assumed to be ON-OFF keying (OOK) modulated before being multiplied by an arbitrary IR-UWB signalling waveform, denoted by $x(t)$.

For OOK modulation, the probability of bit error is given by [28]

$$P_{\text{OOK}} = Q\left(\sqrt{\frac{\alpha S_x}{\sigma_n^2}}\right) \tag{26}$$

where $S_x = \int_{-\infty}^{\infty} |x(t)|^2 dt$ is the transmitted IR-UWB signal power, α is the loss experienced by the IR-UWB signal in the FSPL channel, and σ_n^2 is the power of the AWGN that corrupts the IR-UWB signal at the receiver front-end. In FSPL channels, α is given by $\alpha = (G_{\text{TX}} G_{\text{RX}} 4\pi D f/c)^2$, where G_{TX} is the gain of the TX antenna, G_{RX} is the gain of the RX antenna, D is the TX–RX antenna separation, and $c = 3 \times 10^8$ m/s is the speed of light. The power of the AWGN is given by $\sigma_n^2 = N_o B_s$, where $B_s = f_H - f_L$ and N_o is the PSD of the AWGN process. Applying Parserval's theorem to S_x in (24), the ratio $\alpha S_x/\sigma_n^2$, defined as the SNR at the receiver side and denoted by $\overline{\text{SNR}}$, is expressed as follows:

$$\overline{\text{SNR}} = \frac{\alpha}{2\pi N_o B_s} \int_{-\infty}^{\infty} |X(j\omega)|^2 d\omega = \frac{2\alpha}{N_o \Omega} \int_{\omega_L}^{\omega_H} |X(j\omega)|^2 d\omega \tag{27}$$

where $X(j\omega)$ is the Fourier transform of $x(t)$. Multiplying both sides of (25) by $\max\{S_{\text{FCC}}(\omega)\}$ yields

$$\overline{\text{SNR}} = 2\alpha\eta_x \left(\frac{\max\{S_{\text{FCC}}(\omega)\}}{N_o}\right) \tag{28}$$

where $\eta_x = \int_{\omega_L}^{\omega_H} |X(j\omega)|^2 d\omega / \max\{S_{\text{FCC}}(\omega)\}\Omega = \int_{\omega_L}^{\omega_H} |X(j\omega)|^2 d\omega / \int_{\omega_L}^{\omega_H} S_{\text{FCC}}(\omega)\, d\omega$ is the PE of the generalized IR-UWB signalling waveform; $x(t)$. Substituting (28) in (26) yields

$$P_{\text{OOK}} = Q\left(\sqrt{2\alpha r \eta_x}\right) \tag{29}$$

where $r = \max\{S_{\text{FCC}}(\omega)\}/N_o$ is the ratio of the FCC PSD to the PSD of the AWGN. It is important to highlight that the BER performance of any modulation schemes, including the OOK scheme, is always given in terms of the SNR at the receiver side [28]. Consequently, the SNR expression provided in (28) constitute a unifying metric to evaluate the BER performances expected from differently implemented MWP-based IR-UWB waveform generators in terms of the PE of the produced IR-UWB waveforms. For numerical comparisons, α is calculated at the center frequency of the useful UWB band (i.e., $f = f_o = (\omega_L + \omega_H)/4\pi$). Moreover, antenna gains of $G_{\text{TX}} = G_{\text{RX}} = 1$ and a typical TX–RX separation distance of $D = 4$ m are assumed. The AWGN PSD is given by $N_o = k_B T$, where $k_B = 1.38 \times 10^{-23}$ J/K is the Boltzmann constant and T is the temperature in Kelvin. Based on (29), Fig. 7 shows the BER performances achieved by the IR-UWB waveforms reported in [11]–[17] as compared to the BERs achieved by the optimal Gaussian and sech monocycle waveforms reported in this work. As expected, overall, the higher is the PE, the lower is the achieved BER value. An IR-UWB signaling waveform is judged as power efficient if the forward error correction (FEC) BER limit of 10^{-3} is achieved using this waveform. Clearly, the proposed optimal Gaussian and sech monocycle pulses outperforms the waveforms reported in [11]–[17] in terms of achieving the FEC BER limit, considering their low complexity of generation. Similar results can be inferred when different transmission distances and modulation schemes are assumed.

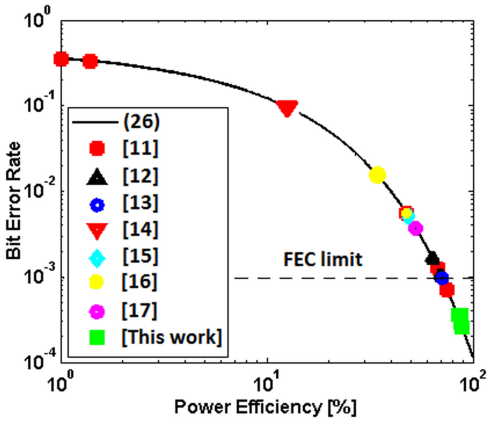

Fig. 7. BER performances achieved by the IR-UWB waveforms reported in [11]–[17] compared to the BERs achievable by single derivative order Gaussian and sech-based waveforms with optimized pulsewidths reported in this work. A unique marker and color combination is dedicated to all IR-UWB waveform designs reported in the same reference. Waveforms belonging to the same reference are discriminated by their individual PEs, which are arranged in an ascending order.

VIII. Design Insights

This section introduces a number of useful simulation and design guidelines, based on the results obtained. The proposed guidelines are summarized as follows.

1) First, the proper pulse shape for the input basis function of an IR-UWB waveform should be identified or at least hypothesized. Second, the net derivative order m offered by the photonic generation technique should be calculated.
2) Pulse shape requirements: Since sech-based IR-UWB waveforms outperform their Gaussian-based counterparts in terms of the maximum achievable data rate and PE, it is recommended to use optical sources that emit the basis function of waveform types, such as MLFLs.
3) Pulsewidth requirements: It is necessary to apply input basis functions with the optimal FWHM pulsewidths of the relevant pulse shape and order. The pulse spreading introduced by optical fibers due to their chromatic dispersion effects should be calculated *a priori* such that an optimum pulsewidth, and consequently, an optimal PE, is obtained at the output fiber end.
4) Pulse amplitude requirements: It is important to compensate for the possible net gain and/or attenuation introduced by the active components in the IR-UWB system such that PSD of the radiated IR-UWB waveform respects the maximum PSD constraints imposed by the FCC spectral mask.
5) Pulse order requirements: The combined differentiation/integration orders introduced by electrical/optical effects to an IR-UWB waveform should be balanced such that the resulting electrical IR-UWB waveform at the PD output is equivalent to a monocycle pulse.
6) Bandwidth requirements: For Gaussian-based IR-UWB waveforms, it is important to secure a minimum effective bandwidth of about 960 MHz, whereas for sech-based IR-UWB waveforms, a minimum effective bandwidth of 1 GHz is required, otherwise; all IR-UWB waveforms are equivalent from an PE perspective and it becomes redundant to aim at generating IR-UWB waveforms of orders higher than a monocycle pulse.
7) FCC fully compliant IR-UWB waveforms: Despite their high PEs, throughout this work, an ideal BPF is assumed to achieve the FCC compliance of the proposed IR-UWB optimal waveforms. In practice, this ideal full compliance might be violated by the leakage PSD of the designed IR-UWB waveforms out of the useful UWB band due to nonideal bandpass filtering. However, the projection onto the convex sets algorithm reported in [29] can be applied to the proposed waveforms to achieve the full compliance to the FCC mask constraints using FIR filtering.
8) System design parameters: The practical system design parameters set Θ should be optimized to achieve the above-mentioned guidelines.

These design guidelines should be followed during the design phase of MWP-based IR-UWB waveform generators if an optimal performance is desired.

IX. Conclusion

In this paper, the performance upper bounds of MWP-assisted UWB waveform generators are evaluated, with the PE of the produced UWB waveforms as the performance metric of interest. Analytical expressions are developed for these upper bounds, based on the introduced configuration and mathematical modeling, and are applied to two practical designs for MWP filters. Moreover, two typical types of IR-UWB waveforms are considered. Numerical simulations confirm the practical applicability of the derived expressions, especially when a fast and close-to-accurate pre/post prototyping performance assessment is desired. The model abstraction level introduced in this work enables MWP system designers to simulate and evaluate their designs rapidly, using general purpose programming languages without the need for specialized photonic software simulation tools.

References

[1] Federal Communications Commission , "First report and order, (part 15 of the commission's rules regarding ultra-wideband transmission systems), US. Fed. Commun. Commission, Rep. DA 02-1658, 2002.
[2] M. Ghavami, L. B. Michal, and R. Kohno, *Ultra Wide Band Signals and Systems in Communication Engineering*. West Sussex, U.K.: Wiley, 2007.
[3] M. G. Di Benedetto and B. Vojcic, "Ultra-wideband wireless communications: A Tutorial," *J. Commun. Netw.*, vol. 5, no. 4, pp. 290–302, Dec. 2003.
[4] X. Wu, Z. Tian, T. N. Davidson, and G. B. Giannakis, "Optimal waveform design for UWB radios," *IEEE Trans. Signal Process.*, vol. 54, no. 6, pp. 2009–2021, Jun. 2006.
[5] J. Yao, F. Zeng, and Q. Wang, "Photonic generation of ultrawideband signals," *J. Lightw. Technol.*, vol. 25, no. 11, pp. 3219–3235, Nov. 2007.
[6] Q. Wang and J. Yao, "An electrically switchable optical ultrawideband pulse generator," *J. Lightw. Technol.*, vol. 25, no. 11, pp. 3626–3633, Nov. 2007.
[7] Q. Wang and J. Yao, "Ultra-wideband Gaussian monocycle and doublet pulse generation using a reconfigurable photonic microwave delay-line filter," in *Proc. IEEE Radio Wireless Symp.*, Jan. 2008, pp. 129–132.
[8] J. Li, B. P.-P. Kuo, and K. K.-Y. Wong, "Ultra-wideband pulse generation based on cross-gain modulation in fiber optical parametric amplifier," *IEEE Photon. Technol. Lett.*, vol. 21, no. 4, pp. 212–214, Feb. 2009.

[9] M. Bolea, J. Mora, B. Ortega, and J. Capmany, "Optical UWB pulse generation using an N tap microwave photonic filter and phase inversion adaptable to different pulse modulation formats," *Opt. Express*, vol. 17, no. 7, pp. 5023–5032, Mar. 2009.

[10] B. Luo, J. Dong, Y. Yu, and X. Zhang, "Bandwidth-tunable single-carrier UWB monocycle generation using a nonlinear optical loop mirror," *IEEE Photon. Technol. Lett.*, vol. 24, no. 18, pp. 1646–1649, Sep. 2012.

[11] M. Abtahi, J. Magne, M. Mirshafiei, L. A. Rusch, and S. LaRochelle, "Generation of power-efficient FCC-compliant UWB waveforms using FBGs: Analysis and experiment," *J. Lightw. Technol.*, vol. 26, no. 5, pp. 628–635, Mar. 2008.

[12] M. Abtahi, M. Mirshafiei, S. LaRochelle, and L. Rusch, "All-optical 500-Mb/s UWB transceiver: An experimental demonstration," *J. Lightw. Technol.*, vol. 26, no. 15, pp. 2795–2802, Aug. 2008.

[13] M. Mirshafiei, M. Abtahi, P. Larochelle, and L. A. Rusch, "Pulse shapes that outperform traditional UWB antenna/waveform combinations," in *Proc. IEEE Global Telecommun. Conf.*, Dec. 2010, pp. 1–5.

[14] S. T. Abraha, C. M. Okonkwo, E. Tangdiongga, and A. M. J. Koonen, "Power-efficient impulse radio ultrawideband pulse generator based on the linear sum of modified doublet pulses," *Opt. Lett.*, vol. 36, no. 12, pp. 2363–2365, Jun. 2011.

[15] S. T. Abraha *et al.*, "Performance evaluation of IR-UWB in short-range fiber communication using linear combination of monocycles," *J. Lightw. Technol.*, vol. 29, no. 8, pp. 1143–1151, Apr. 2011.

[16] P. Li, H. Chen, M. Chen, and S. Xie, "Gigabit/s photonic generation, modulation, and transmission for a reconfigurable impulse radio UWB over fiber system," *IEEE Photon. J.*, vol. 4, no. 3, pp. 805–816, Jun. 2012.

[17] P. Li, H. Chen, X. Wang, H. Yu, M. Chen, and S. Xie, "Photonic generation and transmission of 2-Gbit/s power-efficient IR-UWB signals employing and electro-optic phase modulator," *IEEE Photon. Technol. Lett.*, vol. 25, no. 2, pp. 144–146, Jan. 2013.

[18] M. Malekizandi, Q. T. Le, A. Emsia, D. Briggmann, A. Chipouline, and F. Küppers, "TDM-PON compatible generation of 10 Gbps NRZ and 1.25 Gbps UWB signals by a single light source," *Opt. Express*, vol. 24, no. 15, pp. 17018–17026, 2016.

[19] M. Malekizandi, A. Chipouline, and F. Küppers, "Bidirectional UWB over fiber for WDM-PON system," *Opt. Express*, vol. 25, no. 6, pp. 6840–6850, 2017.

[20] H. Taki, S. Azou, A. Hamie, A. Al Housseini, A. Alaeddine, and A. Sharaiha, "On phaser-based processing of impulse radio UWB over fiber systems employing SOA," *Opt. Fiber Technol.*, vol. 36, pp. 33–40, 2017.

[21] Y. M. Chang, J. Lee, H.-S. Lee, L. Yan, and J. H. Lee, "Generation and distribution of 1.25 Gb/s ultrawideband doublet pulses based on the combination of nonlinear polarization rotation and parametric amplification," *J. Lightw. Technol.*, vol. 29, no. 6, pp. 931–938, Mar. 2011.

[22] J. Lee, Y. M. Chang, and J. H. Lee, "UWB doublet pulse generation using the combination of parametric amplification and cross phase modulation," in *Proc. IEEE Photon. Conf.*, Sep. 2012, pp. 584–585.

[23] Y. M. Chang, J. Lee, and J. H. Lee, "Generation of ultra-wideband doublet pulses based on Kerr shutter using an elliptically polarized beam in Bismuth oxide-based nonlinear optical fiber," in *Proc. Opt. Fiber Commun. Conf. Expo., Nat. Fiber Optic Engineers Conf.*, Mar. 2011, pp. 1–3.

[24] A. Zadok, X. Wu, J. Sendowski, A. Yariv, and A. E. Willner, "Reconfigurable generation of high-order ultra-wideband waveforms using edge detection," *J. Lightw. Technol.*, vol. 28, no. 16, pp. 2207–2212, Aug. 2010.

[25] E. Zhou, X. Xu, K. S. Lui, and K. K. Y. Wong, "Photonic ultrawideband pulse generation with HNL-DSF-based phase and intensity modulator," *IEEE Photon. Technol. Lett.*, vol. 23, no. 7, pp. 396–398, Apr. 2011.

[26] C. Finol and M. Wojtowicz, "Cauchy-Schwarz and Holder's inequalities are equivalent," *Divulgaciones Matematicas*, vol. 15, no. 2, pp. 143–147, 2007.

[27] S. Pan and J. Yao, "IR-UWB-over-fiber systems compatible with WDM-PON networks," *J. Lightw. Technol.*, vol. 29, no. 20, pp. 3025–3034, Oct. 2011.

[28] O. Abedi and M. C. E. Yagoub, "Performance comparison of UWB pulse modulation schemes under white Gaussian noise channels," *Int. J. Microw. Sci. Technol.*, vol. 29, no. 20, pp. 3025–3034, Oct. 2011.

[29] S. Sharma and V. Bhatia, "UWB pulse design using constraint convex sets method," *Int. J. Commun. Syst.*, vol. 30, no. 14, pp. 1–14, Sep. 2017.